

Optical functions and electronic structure of CuInSe₂, CuGaSe₂, CuInS₂, and CuGaS₂

M. I. Alonso,^{1,*} K. Wakita,² J. Pascual,³ M. Garriga,¹ and N. Yamamoto²

¹*Institut de Ciència de Materials de Barcelona, CSIC, Campus de la UAB, 08193 Bellaterra, Spain*

²*Department of Physics and Electronics, College of Engineering,*

Osaka Prefecture University, Gakuen-cho 1-1, Sakai, Osaka 599-8531, Japan

³*Departament de Física, UAB, and Institut de Ciència de Materials de Barcelona, CSIC, 08193 Bellaterra, Spain*

(Dated: October 22, 2018)

We report on the complex dielectric tensor components of four chalcopyrite semiconductors in the optical energy range (1.4–5.2 eV, from 0.9 eV for CuInSe₂) determined at room temperature by spectroscopic ellipsometry. Our results were obtained on single crystals of CuInSe₂, CuGaSe₂, CuInS₂, and CuGaS₂. Values of refractive indices n , extinction coefficients k and normal-incidence reflectivity R in the two different polarizations are given and compared with earlier data where available. We analyze in detail the structures of the dielectric function observed in the studied energy region. Critical-point parameters of electronic transitions are obtained from fitting of numerically calculated second-derivative spectra $d^2\varepsilon(\omega)/d\omega^2$. Experimental energies and polarizations are discussed on the basis of published band structure calculations.

PACS numbers: 78.20.Ci, 71.20.Nr, 78.20.Fm, 07.60.Fs

I. INTRODUCTION

The studied ternary compounds Cu-III-VI₂ (III = Ga, In and VI = S, Se) are direct gap semiconductors with tetragonal chalcopyrite (CH) crystal structure. This family of materials is relevant in many fields, including nonlinear optics, optoelectronic, and photovoltaic devices.^{1,2,3,4} Accurate knowledge of the optical functions of these materials is very important for many of these applications. In spite of the considerable amount of research devoted to these materials, this knowledge is still incomplete. In this paper, we present careful ellipsometric measurements over the energy range 1.4 to 5.2 eV (from 0.9 eV for CuInSe₂) that provide values of the complex dielectric functions $\varepsilon(\omega) = \varepsilon_1(\omega) + i\varepsilon_2(\omega)$ both in the ordinary and extraordinary polarizations. We discuss our results taking into account previous related work.

Another concern of this work is the understanding of the electronic structure of these compounds, especially focusing on the origin of the interband transitions above the band gap. Energies and selection rules of the transitions, both observed in this work and reported in the literature for the different studied compounds, are discussed. As basis, we consider the band structure calculations of Jaffe and Zunger⁵ using a self-consistent approach within the density-functional formalism. We find common trends in the spectra of the four compounds, in agreement with the mentioned calculation.⁵ Despite the large influence of Cu-3*d* states on the electronic band structure, the main optical transitions are shown to originate between hybridized bands. Thus, these spectra bear a rather close relationship with those of binary zinc blende (ZB) compounds in general.

The paper is organized as follows. After a short description of the experiments in Sect. II, the results are presented in the next two Sections. First, in Sect. III, we report and discuss the values of the optical functions of the four compounds. In Sect. IV we analyze in de-

tail the structures of the dielectric function observed in the studied energy region. Then, in Sect. V we relate the critical-point energies to the electronic band structures of the compounds. Finally, we summarize the most important results in Sect. VI.

II. EXPERIMENTAL DETAILS

The samples used in this study were single crystals. In the case of CuInSe₂ we measured a platelet with (112) orientation grown by chemical iodine-vapor transport (IT). The other three samples consisted of (001) oriented faces cut from ingots grown by the traveling-heater method (THM). The THM process requires use of a solvent that may incorporate as impurity in the resulting crystal. In this case, use of In solvent yielded crystals of CuGa_{1-x}In_x(S,Se)₂ with small In contents x , and stoichiometric CuInS₂. We have paid special attention to the problem of removing surface overlayers, which is of primary importance in spectroellipsometric measurements. We used the accepted criteria of Aspnes and Studna⁶ to determine the optically “best” surfaces to obtain dielectric function values representative of bulk semiconductors. The best results for the IT-CuInSe₂ sample were obtained after etching of the as-grown surface in a solution of 5% hydrofluoric acid in de-ionized water. The THM crystals were sequentially polished with slurries of successively finer alumina powder (down to 0.3 μm grid size) in de-ionized water on suitable polishing cloths. Immediately before spectroscopic ellipsometry (SE) measurements, samples were chemomechanically polished with an alkaline colloidal silica suspension (Buehler’s Mastermet), rinsed with de-ionized water, and blown dry with N₂. Variations of this procedure, such as rinsing with methanol instead of water, or further chemical etching of the surface, either did not modify or led to worse spectra, showing both lower $\langle\varepsilon\rangle$ values⁶ and broader spectral

features.

Measurements were done using a spectral ellipsometer with rotating polarizer, at room temperature, and keeping the sample under dry N_2 flux to delay surface contamination. Depending on the sample, more or less degradation was observable after several hours. The spectral range of all measurements was 1.4 to 5.2 eV and for CuInSe_2 we also measured the bandgap region down to 0.9 eV, using a GaInAs photodiode as detector. In all spectral measurements, the angle of incidence was $\varphi = 65^\circ$ and the analyzer azimuth $A = 20^\circ$. The experimental energy step was generally 20 meV, but we used finer meshes of 2 to 10 meV for the sharper gap features. In the THM crystals we acquired two spectra with the plane of incidence either parallel or perpendicular to the in-plane optical axis, characterized by x-ray diffraction. The orientation of the IT sample was checked optically by β -scan measurements⁷ to determine the needed projection of the direction of the c axis on the sample surface. We measured β -scans at two energies with pronounced anisotropy (2.8 and 4 eV) and three analyzer settings (5, 10, and 30 degrees). The obtained results followed well the behavior of a uniaxial crystal with its optic axis forming an angle α with the surface normal. The fitted angle was $\alpha = 55 \pm 1^\circ$, in good agreement with a (112) surface and optic axis along [001]. For this sample we took four spectral measurements at Euler's angles $\beta = 0, 90, 180,$ and 270 degrees to extract the tensor components. Both if the optic axis is on the sample surface or not, there is no direct analytical expression relating the dielectric tensor with the measured spectra. Hence, a numerical inversion of the ellipsometric equations and fit to experimental data was performed for all samples.^{8,9}

III. DIELECTRIC FUNCTION DATA

In this section, we give the dielectric tensors obtained by ellipsometry for each compound. In general, our data are consistent with refractive index measurements done by prism minimum deviation methods in the transparency range of three of the compounds.^{10,11} We compare our results to earlier ellipsometric measurements when available, and also with results of normal-incidence reflectivity R . Our interpretation of the spectra regarding transition energies will be given in Sect. V.

A. CuInSe_2

From the four investigated compounds, CuInSe_2 has been the most studied due to its applicability to photovoltaic devices. Understanding and modeling of solar cell performance requires a thorough knowledge of the fundamental optical properties. For this reason, several ellipsometric studies of CuInSe_2 have already been undertaken.^{12,13,14,15,16} The most complete is the recent publication by Kawashima et al.,¹² where polarized spec-

tra from 1.2 to 5.3 eV are given. However, the important region of the fundamental gap is outside this energy range. Therefore, we show our results including the gap region in Fig. 1. We have checked Kramers-Kronig consistency⁶ of these data to be better than $\pm 0.5\%$, with larger residual structure of $\pm 2\%$ at bandgap. The refractive indices and extinction coefficients obtained in both polarizations are listed in Table I each 0.1 eV. Precision and accuracy of $\langle \varepsilon_2 \rangle$ in spectral regions of small absorption are poor.⁶ Therefore, values of k lower than 0.1 are considered inaccurate and are left blank.

Unpolarized measurements including the gap region were previously presented by Hidalgo et al.,¹⁶ but their reported values of refractive indices were somewhat low, indicative of the presence of surface overlayers. These authors etched their samples in a Br-methanol solution, which according to our experience does not produce the best ellipsometric spectra for CuInSe_2 , as already said in Sect. II. References 14 and 15 both give much too low refractive indices, probably due to lack of attention to sample surface quality. On the contrary, in the work by Kazmerski et al.,¹³ rather accurate values were obtained at several single wavelengths between 546 and 750 nm by correcting the ellipsometric measurements for a surface layer of native In_2O_3 oxide. The estimations of n below bandgap of Sobotta et al.¹⁷ are between 2.9 and 3.0 at 0.8 eV, in fair agreement with our data. Finally, in the region above 1.2 eV, we obtain rather similar spectra to those of Ref. 12, with only minor differences.

The spectra of normal-incidence reflectivity R in both polarizations, calculated from n and k values of Table I, are plotted in Fig. 2. The labeling of the transitions has been chosen in relationship to standard ZB notation and will be discussed in Sect. V. In the literature, there are several measurements of R of CuInSe_2 , either without^{18,19,20} or with²¹ polarization dependence. Except for the measurement by Turowski et al.²⁰ where the values of R are quite low, the other measurements show good R levels, only a bit low towards the UV regions. The two measurements at liquid nitrogen temperature^{19,21} start at 2 eV and cover a broader UV range than our data, therefore they are quite informative in terms of observed interband transitions. In the common energy range, we observe similar structures and polarizations than Austin et al.²¹

B. CuGaSe_2

Refractive index data of CuGaSe_2 have been reported by Boyd et al.¹⁰ in the transparency range of the compound by prism minimum deviation angle measurement. Kawashima et al.¹² have determined the dielectric tensor of CuGaSe_2 from 1.2 to 5.3 eV. There is another ellipsometric measurement by Bottomley et al.¹⁵ that suffers from the same shortcoming already mentioned (see Sect. III A), namely, an optically deficient sample surface. Therefore, it cannot be taken into consideration for

the following discussion.

In the overlapping energy region between 1.2 and 1.6 eV, the two mentioned sets of refractive indices (Refs. 10 and 12) differ by about 0.08. Also, while Boyd's¹⁰ birefringence is considerable, it is insignificant in the measurement of Kawashima.¹² It seems possible that this discrepancy stems from the presence of In impurities in the THM crystal used in Ref. 12. However, our measurement also of a THM crystal, shown in Fig. 3, agrees best with Boyd et al. data in both magnitudes (n and birefringence). Our spectra of ϵ and R display clear and sharp structures, in contrast with those of Ref. 12, thus a possible explanation of the difference is that the In content of our THM sample is smaller than theirs.

Our values of n and k are listed in Table II, where inaccurate data of $k < 0.1$ have been omitted. Overall Kramers-Kronig consistency of the dielectric functions is better than $\pm 0.3\%$ and somewhat larger ($\pm 1\%$) around bandgap. Figure 4 displays the polarized reflectivities calculated from our data. The transitions are labeled according to the assignments done in Sect. V. There are two published measurements of R of this compound which show lower values. The unpolarized spectrum at room temperature of Turowski et al.²⁰ up to 8 eV shows many structures but it gives too low R values and is quite deformed above 4 eV. The polarized spectra measured at low temperature by Matveev et al.²² are somewhat better but are restricted to the 1.7 to 4.5 eV energy range.

C. CuInS₂

The optical properties of CuInS₂ in the range of transparency of the compound have been investigated by Boyd et al.¹¹ In the opaque region, polarized reflectivity spectra around the gap have been reported by Makarova et al.²³ and in a wider energy range by Syrbu et al.,²⁴ both at room and liquid nitrogen temperatures.

Figure 5 shows the result of our measurements together with data taken from Ref. 11. There is no overlap between both sets of data but the endpoints just coincide. As it is seen in Fig. 5, the values of $\langle \epsilon_1 \rangle$ and therefore of refractive index do not join smoothly. Our values of n listed in Table III are about 0.05 higher and our birefringence $\Delta n = n_{\parallel} - n_{\perp}$ is slightly smaller. Also, the absorption edge in our crystal is located at lower energy. Although the origin of these differences is not clear, they may be caused by a variation of stoichiometry.²⁵ Kramers-Kronig consistency of the dielectric functions in this case is quite good ($\pm 0.1\%$), increasing to about 1% at the edges of the spectra.

Our reflectivity, given in Fig. 6, is higher than those reported earlier. This is due to careful surface preparation. In Ref. 23 the authors measured $n = 2.55$ and $k = 0.59$ by ellipsometry at 1.96 eV (He-Ne laser). These values are clearly indicative of an optically not abrupt surface, in spite that the sample was freshly polished and etched in CCl₄ prior to the measurement. Therefore, this treat-

ment does not seem quite adequate. The R spectra of Syrbu et al.²⁴ show somewhat low values. Nevertheless, these spectra contain fine structure even at room temperature. The gross features resemble those seen in our spectra.

D. CuGaS₂

The optical properties of CuGaS₂ have been reviewed recently by Rife.²⁶ Refractive indices in the transparency range were measured by Boyd et al.¹¹ At higher energies, from 2.5 to 26 eV, the optical functions²⁶ were calculated from Kramers-Kronig analysis of reflectivity data measured at 80 K.¹⁹ Comparing our results with those available data we find very good agreement with Boyd et al.¹¹ (see Fig. 7). Our values of n , given in Table IV, are slightly higher and the birefringence smaller due to the small In content of our crystal. On the contrary, the optical functions in the opaque range given by Rife²⁶ are substantially different from our data. In the overlap region our values of n are a 15% higher in average, discounting excitonic peaks. Also, our value of k above gap (f. i., at 3 eV) is approximately a factor of 2 smaller than given in Ref. 26. These differences can be caused by the original values of R used¹⁹ that are 8 to 10% lower (excepting prominent structures) relative to the R calculated from our data and shown in Fig. 8. The different sample temperature of the measurements is not likely to produce these differences. For instance, dispersion of birefringence of CuGaS₂ near the absorption edge does not vary much between room and liquid He temperatures,²⁷ the largest difference in behavior being given by the shift of the band gap.

The spectra shown in Fig. 7 are consistent under Kramers-Kronig transformations within $\pm 0.5\%$, with larger residual structures of $\pm 1\%$ at the band gaps. Concerning the structures observed in the spectra, the R spectra of Rife et al.¹⁹ at 80 K comprise a wide energy range, thus giving important information about electronic transition energies.

IV. CRITICAL POINT ANALYSIS

Different aspects of the optical and electronic properties of Cu-III-VI₂ compounds have been investigated by several groups. Here we concentrate on the optical transition energies and their relationship to the electronic band structure. The band structure calculations of Jaffe and Zunger^{5,28} provide a theoretical reference framework for these class of compounds. However, from the experimental point of view, such a comprehensive framework is missing. The structure of the fundamental absorption edge is quite well understood but no unanimous interpretation of the upper transitions has yet been established. In part, this is due to the fact that many experimental works were done before the mentioned *ab-initio* calcula-

tions could be realized. But, in addition, studies done after those calculations, have seldom attempted to assign the optical transitions above the fundamental edge. Also, some of the assignments were done without taking into account the selection rules of the transitions. In this work, we admit the complexity of such assignments, but we look for general trends in the spectra and give a consistent view that agrees with symmetry arguments.

The dielectric function of a semiconductor is closely linked to its electronic band structure. The features observed in $\varepsilon(\omega)$ at optical energies are related to interband transitions characterized by large or singular joint density of states (DOS), i. e., critical points (CPs). The behavior of $\varepsilon(\omega)$ near a CP is given by^{29,30}

$$\varepsilon(\omega) = C - Ae^{i\phi}(\omega - E + i\gamma)^n, \quad (1)$$

where A is the amplitude, ϕ the phase angle, E the energy threshold, and γ the broadening. The exponent n takes the values $-\frac{1}{2}$, 0, and $\frac{1}{2}$ for one (1D), two (2D), and three-dimensional (3D) CPs, respectively. Discrete excitons (0D) are represented by $n = -1$. Conclusions about the bands can be drawn by evaluating experimental $\langle\varepsilon(\omega)\rangle$ spectra using Eq. 1 to determine CP parameters. Usually, fitting procedures are run on numerically calculated derivatives of $\langle\varepsilon(\omega)\rangle$. Here, we have calculated the $d^2\langle\varepsilon\rangle/d\omega^2$ of our experimental tensor components using the standard technique of smoothing polynomials.³⁰ Appropriate polynomial degree and number of correlated points were chosen to avoid line shape distortion while giving the best possible structure enhancement. For the fundamental band gap features the best fits were obtained with excitonic line shapes for all three transitions. For the other strong structures, 2D line shapes were suitable. Then, for weaker structures, 2D line shapes were used as well. The obtained derivatives along with their best fits are presented in Figs. 9 to 12.

As it happens with the spectra of $\langle\varepsilon(\omega)\rangle$, the second-derivative spectra of both selenides (Figs. 9 and 10) bear close resemblance to each other, as do both sulfides (Figs. 11 and 12). At room temperature, the former spectra display more prominent structures than the latter. In general, spectra of ordinary polarization ($\mathbf{E} \perp c$) contain more structure than the extraordinary ones ($\mathbf{E} \parallel c$), except in the case of CuInS_2 where there is only partial polarization selectivity and all transitions are present in both polarizations. However, the general traits of all four spectra are alike. A closer consideration of the electronic structure of these compounds is needed in order to look for plausible assignments for the observed transitions.

V. ELECTRONIC STRUCTURE: ASSIGNMENTS AND DISCUSSION

A. Particularities of the electronic structure

Ternary chalcopyrites I-III-VI₂ can be viewed as isolectronic analogs of the II-VI binary semiconductors. The

symmetry reduction given by the chemical difference between the two cations, combined with the two structural modifications η (tetragonal distortion of the unit cell) and u (anion displacement from the ideal tetragonal site) result in a richer range of physical and chemical properties than their binary analogs. Intricacy is further enhanced in Cu-III-VI₂ compounds where noble-atom d orbitals strongly participate in bonding through hybridization with the anion sp states.

In the simplest approach where only symmetry differences are considered, the electronic structure of CH can be derived from that of ZB binary analogs.³¹ The Bravais lattice of CH is shown in Fig. 13. The corresponding elementary cell contains eight atoms ($\text{Cu}_2\text{-III}_2\text{-VI}_4$) instead of the two found in the binaries. Consequently the Brillouin zone reduces its volume by a factor of four. Sets of four different wavevectors of the original ZB Brillouin zone fold into a single point of the new, four times smaller, CH Brillouin zone. Both Brillouin zones are depicted in Fig. 14. The main symmetry points of the CH Brillouin zone are (in units of π/a): $\Gamma(000)$ with states originated in $\Gamma(000)$, $X(002)$, $W(201)$, and $W(021)$; $T(001)$ with states from $\Delta(001)$, $\Delta(00\bar{1})$, $X(200)$, and $X(020)$; and $N(110)$ with states from $L(111)$, $L(\bar{1}\bar{1}1)$, $\Sigma(1\bar{1}0)$, and $\Sigma(\bar{1}10)$. This change in symmetry also forces degeneracy of some electronic states, either directly (N states are always doubly degenerate) or relating spatially uncoupled electronic states by means of time reversal symmetry [as for $(T_1 + T_2)$ and $(T_3 + T_4)$]. At the same time some existing degeneracies of the ZB electronic states are apt to be lifted.

The relevance of these symmetry facts depends on the actual value of the tetragonal interaction. The crystal field breaks the degeneracy of the topmost valence band states and induces the splitting of the ZB Δ states at the new T Brillouin zone edge states. The details of tetragonal distortion effects on the symmetry of electronic states with energies close to the fundamental band gap are given in Fig. 15. For convenience, in the remaining part of this work, we shall term B[A] for the link between k -points A and B, in ZB and CH compounds, respectively.

The tetragonal perturbation also changes the interaction between atomic states that compose the valence and conduction bands. In a wide-gap II-VI semiconductor the valence band is mainly built from s and p states of the VI-anion. The s states form a band at about 11 eV below the topmost valence band³² and are therefore irrelevant for the experimental energy range considered in this work. The p states span a range of about 5 eV. In the binary analogs these states have Γ_{15} symmetry or, if lower, compatible with it. For example, at the center of the Brillouin zone, in a CH structure, the valence band states of a II-VI compound have $\Gamma_{15v} + (X_{5v} + X_{3v}) + 2(W_{3v} + W_{2v} + W_{1v})$ symmetry, equivalent to having 4 Γ_{15} . In the ternary Cu-III-VI₂ compounds, Cu- $3d$ states reside in valence band energy range. The d states split into two Γ_{12} and three Γ_{15} states in the tetrahedral ZB symmetry. Only $\Gamma_{15}(d)$ states can interact with the anion p states giv-

ing rise to bonding and antibonding bands, whereas the $\Gamma_{12}(d)$ states form the nonbonding band. The associated DOS of these three bands has been observed in photoemission experiments.^{33,34} If we now reduce the symmetry to that of CH we get new coupling possibilities. At the Brillouin zone center the 12 VI-anion p states (three for each of the four atoms in the elementary cell) reduce to $(\Gamma_{4v} + \Gamma_{5v})[\Gamma_{15v}] + \Gamma_{5v}[X_{5v}] + \Gamma_{2v}[X_{3v}] + \Gamma_{5v}[2W_{3v}] + (\Gamma_{3v} + \Gamma_{4v})[2W_{2v}] + (\Gamma_{1v} + \Gamma_{2v})[2W_{1v}]$, that is $\Gamma_{1v} + 2\Gamma_{2v} + \Gamma_{3v} + \Gamma_{4v} + 3\Gamma_{5v}$. The six $\Gamma_{15}(d)$ Cu states split into $(\Gamma_3 + \Gamma_4 + 2\Gamma_5)$ and the four $\Gamma_{12}(d)$ states into $(\Gamma_1 + \Gamma_2 + \Gamma_3 + \Gamma_4)$. Consequently a coupling between anion p states and $\Gamma_{12}(d)$ states is also possible. If these states have energies that lie near the middle of the valence band, the most sensitive to hybridization would be Γ_2 and Γ_3 states, because they are closer to p states with alike symmetry. The inclusion of Cu-3d states does not change significantly the generic diagram of energy levels displayed in Fig. 15. It merely adds a new fourfold band with small dispersion corresponding to $\Gamma_{12}(d)$ Cu states.

This symmetry predicted scheme for the electronic valence band structure of I-III-VI₂ CHs is confirmed by photoemission spectroscopy^{33,34} and reproduced by theoretical calculations⁵. Both results conclude that the upper valence band is made exclusively by $p - d$ hybridization of Cu and VI group anions, whereas the III group cations do not contribute. Structures in the d -DOS are almost insensitive to substitutions of the III group cation. The strength of $\Gamma_{15}(d)$ - $\Gamma_{15}(p)$ interaction depends inversely on the energy separation between Cu-3d orbitals and VI-anion p orbitals. This repulsive interaction pushes the antibonding $p - d$ states to higher energies and the resulting valence band width is narrower for heavier VI-atoms. Moreover, not all these antibonding $p - d$ states are consumed in the valence band and a significant amount of anion p character exists also at the conduction band. This is obviously accompanied by some hybridized Cu- d character. Tetragonal crystal field leaves the $\Gamma_{12}(d)$ Cu states in a narrow, almost unhybridized band midway of the bonding and antibonding $p - d$ bands.

For a complete description of the system, the atomic spin-orbit interaction should be added. The symmetry analysis would change and the coupling between atomic electronic states would differ accordingly. From the point of view of symmetry, the spin-orbit interaction leads to further level splittings and to less selective polarization dependence of the transitions. However, experimentally, the only manifestation of spin-orbit interaction is the well known fundamental gap triplet (see below) clearly seen in CuGaSe₂. The $p - d$ hybridization is known¹ to reduce the spin-orbit effects relative to the ZB analogs, so that, in sulfides, the effective spin-orbit parameter is very small (see Table V). Because the general traits of the higher transitions look similar for all four compounds studied in this work, we believe that the spin-orbit interaction is not meaningful above the band gap. Therefore, the complexity introduced by the spin-orbit interaction has

been omitted in our subsequent analysis of the optical properties of Cu-III-VI₂ CHs.

B. Properties of the optical transitions

In a first approximation, the optical functions of ternary compounds (see Figs. 1, 3, 5, and 7) are similar to those of the binary analogs. Nevertheless, symmetry differences between ZB and CH structures and the contribution of Cu-3d states to the upper valence band do result in distinctive features in the optical spectra. The main significative traits are described in the following.

The structure of the fundamental absorption edge of these compounds is well known.¹ The crystal field interaction splits the threefold degenerate Γ_{15} valence band maximum, as shown in Fig. 15. Considering besides the spin-orbit interaction, the fundamental gap consists of three transitions $E_0(A) \equiv E_A$, $E_0(B) \equiv E_B$, and $E_0(C) \equiv E_C$. From symmetry arguments only transition $E_0(B)$ is forbidden in $\mathbf{E} \parallel c$ polarization. However, $E_0(A)$ and $E_0(C)$ transitions are mainly seen in $\mathbf{E} \parallel c$ and $\mathbf{E} \perp c$, respectively. The energies and selection rules found from experiment allow to calculate the energetic disposition of the three valence band states and the crystal field (Δ_{cf}) and spin-orbit (Δ_{so}) parameters using the quasicubic model.¹ Compared with the binary analogs, Cu-III-VI₂ ternaries show a significant band gap reduction due to repulsive interaction between Cu-3d states and VI-anion p states.²⁸

Above the fundamental gap, the dielectric function in the binaries is mainly dominated by two strong transitions, E_1 and E_2 , and a third less active response E'_0 .^{39,40} In our description of the interband transitions we follow the standard notation where the numeric subindex describes the Brillouin zone region where the transition originates. In Fig. 15 we show the ZB states involved in those transitions. The E'_0 structure corresponds to the $\Gamma_{15v} \rightarrow \Gamma_{15c}$ transition which in II-VI compounds is usually found above E_1 and E_2 and occurs beyond our experimental range. In the CH structure the Brillouin zone gathers different k -points of a folded ZB Brillouin zone and reduced symmetry can induce electronic transitions that were weak or forbidden in the binaries. Examples are indirect transitions like $\Gamma(000) \rightarrow X(002)$, or the enhanced joint DOS at the $T(001)$ point coming from ZB $\Delta(001) \rightarrow \Delta(001)$. Thus, there is an increase in the number of symmetry allowed interband transitions and consequently the optical spectra of ternary compounds are richer in structure. Several, usually weak, transitions are expected, superimposed on the dominant spectral features (see Figs. 9–12) stemming from E_1 and E_2 transitions of the binary compounds. Another important effect of tetragonal symmetry is polarization selectivity which proves very helpful to assign observed transitions. For instance, transitions at the N point are allowed in both polarizations, whereas transitions involving former ZB X -point states show a strong anisotropy at the Γ and

T points of CH Brillouin zone. The selection rules for dipolar electric transitions at high symmetry points of CH Brillouin zone are summarized in Table VI.

The contribution of Cu-3d states to the upper valence band affects only slightly the optical spectra, its main contribution being the band gap reduction and suppression of spin-orbit effects. Transitions from the nonbonding $\Gamma_{12}(d)$ Cu states to the conduction band are forbidden in the ZB structure, but allowed for the CH structure. Nevertheless, if present, these transitions should be very weak because theoretical calculations⁵ and photoemission experiments^{33,34} show that Γ_{12} states form a very narrow band with a small dispersion induced by the tetragonal interaction.

C. Assignment of optical transitions

In the well-known region of the fundamental gap, our measured transition energies are gathered in Table V along with relevant data published before. Literature results at low temperatures are given in the cases where small splittings cannot be resolved at room temperature. The energies found in this work for both CuInVI₂ compounds compare well with the reference values. In both cases we find $E_0(A) = E_0(B)$ within experimental error, as is habitual at room temperature. The gap of 1.04 eV for CuInSe₂ at room temperature is rather high, indicating a proper stoichiometry of the crystal.⁴¹ The gap we measure for CuInS₂ is also a good value; the gap of the best stoichiometric CuInS₂ at room temperature is considered to be 1.535 eV.²⁵ In the two CuGaVI₂ compounds we find slightly reduced gaps and Δ_{cf} parameters due to the small In content of the crystals grown by the THM process. Comparing the measured gaps with the references we estimate a composition CuGa_{0.95}In_{0.05}VI₂ for both crystals.

The transition energies above the fundamental gap obtained from ellipsometry and low temperature polarized reflectivity measurements have been collected in Tables VII and VIII. By inspecting all the spectra, we can establish a general pattern for the outstanding optical transitions above the fundamental gap of the four Cu-III-VI₂ compounds analyzed in this work. In all spectra the first strong transition, called $E_1(A)$, is allowed in both polarizations. At ≈ 0.3 eV above it there is a weaker transition $E(X\Gamma)$ that appears only in perpendicular polarization. About 0.8 eV above $E_1(A)$ there is another optical transition allowed in both polarizations, labeled $E_1(B)$. Nearby, and only in parallel polarization, emerges a transition $E(\Delta X)$, located at ≈ 0.5 eV above (VI = Se) or below (CuGaS₂) $E_1(B)$. Close to 5 eV a strong double structure is observed: $E_2(A)$ and $E_2(B)$ allowed in perpendicular and parallel polarization, respectively. This general pattern is also in agreement with ellipsometric measurements reported for CuAlSe₂.⁴²

We associate transitions $E_1(A)$ and $E_1(B)$ to E_1 -like transitions at the N point of the Brillouin zone. As de-

scribed in Fig. 15, the E_1 transition of binary ZB splits into two $N_{1v} \rightarrow N_{1c}$ transitions in CH. If we identify $E_1(A)$ and $E_1(B)$ with this pair, the splitting between the two N_{1v} involved valence band states would be of the order of 0.8 eV. Due to the proximity of another band coming from Σ points in ZB, theory⁵ gives three close N_{1v} valence band states. Calculated energy differences are of the order of $\Delta E(N_{1v}^{(1)} - N_{1v}^{(2)}) \approx 0.4$ eV and $\Delta E(N_{1v}^{(2)} - N_{1v}^{(3)}) \approx 0.6$ eV (except in CuGaS₂ where they are 0.2 eV and 0.8 eV, respectively). All three possibilities give the correct order of magnitude of the measured 0.8 eV. However, we prefer the assignment of transitions $E_1(A)$ and $E_1(B)$ to the lowest-energy $N_{1v}^{(1)} \rightarrow N_{1c}^{(1)}$ and $N_{1v}^{(2)} \rightarrow N_{1c}^{(1)}$, respectively.

$E(X\Gamma)$ is a new interband transition, only allowed in $\mathbf{E} \perp c$, with no corresponding direct transition in binary compounds. Using the diagram of Fig. 15 the three possible assignments by symmetry are the pseudodirect transitions $E(\Gamma X): \Gamma_{5v}^{(1)}[\Gamma_{15v}] \rightarrow \Gamma_{3c}[X_{1c}]$, $E(X\Gamma): \Gamma_{5v}^{(2)}[X_{5v}] \rightarrow \Gamma_{1c}[\Gamma_{1c}]$, and $E'(\Gamma X): \Gamma_{5v}^{(1)}[\Gamma_{15v}] \rightarrow \Gamma_{2c}[X_{3c}]$. Calculations⁵ predict for most of the four Cu-III-VI₂ compounds energies in the sequence $E(\Gamma X) < E_1(A) < E(X\Gamma) < E'(\Gamma X)$. Following this theoretical prediction, we propose to assign $\Gamma_{5v}^{(2)} \rightarrow \Gamma_{1c}$ to the $E(X\Gamma)$ optical structure. This feature on the high energy side of $E_1(A)$ corresponds to an interband transition between the heavy hole p band and the bottom of the conduction band. Notice also that in all experimental spectra we find a weak shoulder below $E_1(A)$ which is only allowed in $\mathbf{E} \perp c$. We propose to associate this shoulder to the mentioned lower energy $E(\Gamma X)$ optical transition. Also, in the two CuIn-VI₂ compounds there is another transition only allowed in $\mathbf{E} \perp c$ that we assign to $E'(\Gamma X)$.

The structure that appears in $\mathbf{E} \parallel c$ and is labeled $E(\Delta X)$ has no correspondent direct transition in the binary analogues. Taking into account both selection rules and calculated energies,⁵ the only matching transition from the upper valence band to the conduction band would be the pseudodirect transition $(T_{3v} + T_{4v})[\Delta_{3v} + \Delta_{4v}] \rightarrow (T_{1c} + T_{2c})[X_{1c}]$. Yet another possibility could be to associate this structure to electronic transitions from nonbonding $\Gamma_{12}(d)$ states to the minimum of the conduction band at Γ_{1c} . However, if we use the experimental values of measured maximum DOS of nonbonding $\Gamma_{12}(d)$ states^{33,34} to calculate the expected energies of such a transition, we obtain energies that do not coincide with our experimental $E(\Delta X)$, even if we consider broadening effects on $\Gamma_{12}(d)$ states. Also, comparing CuInSe₂ and CuGaSe₂ where this transition is particularly well resolved, the difference between both $E(\Delta X)$ energies should coincide with the difference in band gaps,³⁴ which is not the case. Then, we discard that unhybridized $\Gamma_{12}(d)$ states are involved in this transition and conclude that within the spectral range covered by our experimental set-up, only $p-d$ hybridized anti-bonding valence band states contribute to the main band-to-band electronic transitions.

The four compounds show a high dielectric response and large anisotropy at ≈ 5 eV. In analogy with II-VI compounds, we identify the observed structures $E_2(A)$ and $E_2(B)$ with E_2 transitions. Within the energy range of E_2 transitions, notice that the $X(002)$ point folds to the Γ point, and the other two equivalent points in ZB, $X(200)$ and $X(020)$, fold to the T point. The X direct transition at Γ , $\Gamma_{5v}^{(2)}[X_{5v}] \rightarrow \Gamma_{3c}[X_{1c}]$, is only allowed in perpendicular polarization. On the contrary, $X(200)$ and $X(020)$ states are coupled at T -point. The new electronic states give rise to a pair of direct transitions, $E_2(A)$: $(T_{3v} + T_{4v})[X_{5v}] \rightarrow T_{5c}^{(1)}[X_{1c}]$, and $E_2(B)$: $T_{5v}[2X_{5v}] \rightarrow T_{5c}^{(1)}[X_{1c}]$, allowed in perpendicular and parallel polarization, respectively. Theory predicts for the two valence band states at T , T_{5v} and $(T_{3v} + T_{4v})$, a splitting of about 1–1.5 eV. T_{5v} belongs to the upper antibonding manifold bands while $(T_{3v} + T_{4v})$ belongs to the $p - d$ bonding energy region. According to theoretical predictions, only the transitions $T_{5v} \rightarrow T_{5c}^{(1)}$ would contribute to E_2 (the energy of transition $\Gamma_{5v}^{(2)} \rightarrow \Gamma_{3c}$ is always above that of $T_{5v} \rightarrow T_{5c}^{(1)}$). This seems to be in contradiction with experimental results, which shows that transitions with $\mathbf{E} \parallel c$ are also allowed in this energy region. The discrepancy should be overcome if the splitting of the two valence bands is of ≈ 0.2 eV, much smaller than calculated.⁵ But notice also that at T point, the energy difference between $T_{5c}^{(1)}$, and $(T_{1c} + T_{2c})$, is only of ≈ 0.3 eV (except for CuGaSe₂, which is ≈ 0.03 eV), and the doublet $T_{5v} \rightarrow (T_{1c} + T_{2c})$ (allowed in $\mathbf{E} \perp c$) and $T_{5v} \rightarrow T_{5c}^{(1)}$ (allowed in $\mathbf{E} \parallel c$), can be also a good candidate for $E_2(A)$ and $E_2(B)$ transitions. The proposed assignments and notation of the main optical transitions are given in the generic band structure displayed in Fig. 16. Although we cannot distinguish the origin of the observed features in k -space, the main contributions are drawn at zone center Γ and zone edge N and T points.

VI. SUMMARY

We have presented the dielectric tensor components of the four ternary chalcopyrites CuInSe₂, CuGaSe₂, CuInS₂, and CuGaS₂, measured on single crystal samples at room temperature in the energy range from 1.4 to 5.2 eV (from 0.9 eV for CuInSe₂). The pseudodielectric components have been obtained from complex reflectance ratios measured in appropriate configurations. We have paid special attention to the problem of preparing and maintaining a good sample surface throughout the experiments. Thus, the obtained dielectric function values are representative of the bulk material. This is confirmed by the excellent agreement of our results with those of earlier prism minimum deviation methods in the transparency range of three of the compounds.

In addition, we have obtained the parameters of interband transitions from the numerically differentiated components. In particular, we have identified general trends of the spectra and given assignments for the most important transitions, taking into account band structure calculations and the appropriate selection rules for coupling between electronic states. Within the spectral range covered by our experimental set-up, only $p - d$ hybridized anti-bonding valence band states contribute to the main band-to-band electronic transitions. Hence, the optical spectra of these compounds resemble more than previously assumed those of their ZB analogues.

Both the spectral dependence of the optical functions and the critical point analysis are expected to be useful in further studies of structures based on these compounds.

Acknowledgments

This work has been partially supported by the Spanish CICYT project TIC97-0594.

* Electronic address: Isabel.Alonso@icmab.es

¹ J. L. Shay and J. H. Wernick, *Ternary Chalcopyrite Semiconductors: Growth, Electronic Properties, and Applications* (Pergamon, Oxford, 1975).

² M. C. Ohmer and R. Pandey, *Mat. Res. Bull.* **23**(7), 16 (1998).

³ R. W. Birkmire and E. Eser, *Annu. Rev. Mater. Sci.* **27**, 625 (1997).

⁴ S. Chichibu, S. Shirakata, S. Isomura, and H. Nakanishi, *Jpn. J. Appl. Phys.* **36**, 1703 (1997).

⁵ J. E. Jaffe and A. Zunger, *Phys. Rev. B* **28**, 5822 (1983).

⁶ D. E. Aspnes and A. A. Studna, *Phys. Rev. B* **27**, 985 (1983).

⁷ M. I. Alonso, M. Garriga, F. Alsina, and S. Piñol, *Appl. Phys. Lett.* **67**, 596 (1995).

⁸ R. M. A. Azzam and N. M. Bashara, *Ellipsometry and Polarized Light* (North-Holland, Amsterdam, 1977).

⁹ M. I. Alonso, S. Tortosa, M. Garriga, and S. Piñol, *Phys.*

Rev. B **55**, 3216 (1997).

¹⁰ G. D. Boyd, H. M. Kasper, J. H. McFee, and F. G. Storz, *IEEE J. Quantum Electron.* **8**, 900 (1972).

¹¹ G. D. Boyd, H. Kasper, and J. H. McFee, *IEEE J. Quantum Electron.* **7**, 563 (1971).

¹² T. Kawashima, S. Adachi, H. Miyake, and K. Sugiyama, *J. Appl. Phys.* **84**, 5202 (1998).

¹³ L. L. Kazmerski, M. Hallerdt, P. J. Ireland, R. A. Mickelsen, and W. S. Chen, *J. Vac. Sci. Technol. A* **1**, 395 (1983).

¹⁴ F. A. Abou-Elfotouh, G. S. Horner, T. J. Coutts, and M. W. Wanlass, *Sol. Cells* **30**, 473 (1991).

¹⁵ D. J. Bottomley, A. Mito, S. Niki, and A. Yamada, *J. Appl. Phys.* **82**, 817 (1997).

¹⁶ M. L. Hidalgo, M. Lachab, A. Zouaoui, M. Alhamed, C. Llinares, J. P. Peyrade, and J. Galibert, *Phys. Status Solidi B* **200**, 297 (1997).

¹⁷ H. Sobotta, H. Neumann, V. Riede, G. Kühn, J. Seltmann,

- and D. Oppermann, Phys. Status Solidi A **60**, 531 (1980).
- ¹⁸ J. Gan, J. Tauc, V. G. Lambrecht Jr., and M. Robbins, Solid State Commun. **15**, 605 (1974).
- ¹⁹ J. C. Rife, R. N. Dexter, P. M. Bridenbaugh, and B. W. Veal, Phys. Rev. B **16**, 4491 (1977).
- ²⁰ M. Turowski, A. Kisiel, and R. D. Tomlinson, Nuovo Cimento **2D**, 2064 (1983).
- ²¹ J. Austinat, H. Nelkowski, and W. Schrittenlacher, Solid State Commun. **37**, 285 (1981).
- ²² A. V. Matveev, V. E. Grachev, V. V. Sobolev, and V. E. Tazlavan, Phys. Status Solidi B **194**, K7 (1996).
- ²³ T. L. Makarova, G. A. Medvedkin, Y. V. Rud', and M. A. Tairov, Sov Phys. Tech. Phys. **33**, 975 (1988).
- ²⁴ N. N. Syrbu, R. V. Cretu, and V. E. Tezlevan, Cryst. Res. Technol. **33**, 135 (1998).
- ²⁵ T. M. Hsu, J. Appl. Phys. **59**, 2538 (1986).
- ²⁶ J. C. Rife, in *Handbook of Optical Constants of Solids III*, edited by E. D. Palik (Academic Press, San Diego, 1998), p. 459.
- ²⁷ I.-H. Choi, S.-H. Eom, and P. Y. Yu, J. Appl. Phys. **82**, 3100 (1997).
- ²⁸ J. E. Jaffe and A. Zunger, Phys. Rev. B **29**, 1882 (1984).
- ²⁹ M. Cardona, *Modulation Spectroscopy* (Academic, New York, 1969), p. 1.
- ³⁰ P. Lautenschlager, M. Garriga, S. Logothetidis, and M. Cardona, Phys. Rev. B **35**, 9174 (1987).
- ³¹ J. Camassel, L. Artus, and J. Pascual, Phys. Rev. B **40**, 5717 (1990).
- ³² D. J. Stukel, R. N. Euwema, T. C. Collins, F. Herman, and R. L. Kortum, Phys. Rev. **179**, 740 (1969).
- ³³ K. Takarabe, K. Kawai, S. Minomura, T. Irie, and M. Taniguchi, J. Appl. Phys. **71**, 441 (1992).
- ³⁴ M. Turowski, G. Margaritondo, M. K. Kelly, and R. D. Tomlinson, Phys. Rev. B **31**, 1022 (1985).
- ³⁵ J. L. Shay, B. Tell, H. M. Kasper, and L. M. Shiavone, Phys. Rev. B **7**, 4485 (1973).
- ³⁶ J. L. Shay, B. Tell, H. M. Kasper, and L. M. Shiavone, Phys. Rev. B **5**, 5003 (1972).
- ³⁷ S. Shirakata, S. Chichibu, and S. Isomura, Jpn. J. Appl. Phys. **36**, 7160 (1997).
- ³⁸ H. Horinaka, N. Yamamoto, and T. Miyauchi, Jpn. J. Appl. Phys. **17**, 521 (1978).
- ³⁹ S. Adachi and T. Taguchi, Phys. Rev. B **43**, 9569 (1991).
- ⁴⁰ C. Janowitz, O. Günther, G. Jungk, R. L. Johnson, P. V. Santos, M. Cardona, W. Faschinger, and H. Sitter, Phys. Rev. B **50**, 2181 (1994).
- ⁴¹ S. Shirakata, S. Chichibu, S. Isomura, and H. Nakanishi, Jpn. J. Appl. Phys. **36**, L 543 (1997).
- ⁴² M. I. Alonso, J. Pascual, M. Garriga, Y. Kikuno, N. Yamamoto, and K. Wakita, J. Appl. Phys. **88**, 1923 (2000).

Figures

FIG. 1: Dielectric tensor components of CuInSe₂. The ordinary ($\mathbf{E} \perp c$) functions are plotted with solid lines, and the extraordinary ($\mathbf{E} \parallel c$) with dotted lines. Upper panel (a) shows the real parts, panel (b) the imaginary parts.

FIG. 2: Reflectivity of CuInSe₂ at normal incidence calculated for the two polarizations.

FIG. 3: Ordinary (solid lines) and extraordinary (dashed lines) dielectric tensor components of CuGaSe₂. Upper panel (a) shows the real parts, panel (b) the imaginary parts. Symbols in (a) are data taken from Ref. 10.

FIG. 4: Polarized reflectivities of CuGaSe₂ at normal incidence.

FIG. 5: Ordinary (solid lines) and extraordinary (dashed lines) dielectric tensor components of CuInS₂. Upper panel (a) shows the real parts, panel (b) the imaginary parts. Symbols in (a) are data taken from Ref. 11.

FIG. 6: Polarized reflectivities of CuInS₂ at normal incidence.

FIG. 7: Ordinary (solid lines) and extraordinary (dashed lines) dielectric tensor components of CuGaS₂. Upper panel (a) shows the real parts, panel (b) the imaginary parts. Symbols in (a) are data taken from Ref. 11.

FIG. 8: Polarized reflectivities of CuGaS₂ at normal incidence.

FIG. 9: Second-derivative spectra of CuInSe₂. (a) Ordinary, (b) Extraordinary polarization. Experimental points are plotted by symbols and their best fit is given by lines. The arrows mark the obtained critical-point energies.

FIG. 10: Second-derivative spectra of CuGaSe₂. (a) Ordinary, (b) Extraordinary polarization. Experimental points are plotted by symbols and their best fit is given by lines. The arrows mark the obtained critical-point energies.

FIG. 11: Second-derivative spectra of CuInS₂. (a) Ordinary, (b) Extraordinary polarization. Experimental points are plotted by symbols and their best fit is given by lines. The arrows mark the fitted critical-point energies.

FIG. 12: Second-derivative spectra of CuGaS₂. (a) Ordinary, (b) Extraordinary polarization. Experimental points are plotted by symbols and their best fit is given by lines. The arrows mark the fitted critical-point energies.

FIG. 13: Crystalline chalcopyrite structure Cu-III-VI₂ depicted in real space. It belongs to the space group D_{2d}^{12} and is a superstructure of zinc blende T_d^2 .

FIG. 14: Brillouin zone of chalcopyrite (CH) and its relationship to that of zinc blende (ZB). The volume of the former is four times smaller than that of the latter. The dotted polyhedra show the ZB reciprocal space regions that fold into the CH Brillouin zone. Symmetry points are labelled A_B , where A and B refer to the CH and ZB symmetries, respectively.

FIG. 15: Schematic representation of energy levels and their symmetry in zinc blende (ZB) and chalcopyrite (CH) structures.

FIG. 16: Proposed assignments and notations for the transitions observed in Cu-III-VI₂ chalcopyrites in the optical range, depicted on a generic band structure. Dashed and solid arrows represent optical transitions allowed in $\mathbf{E} \parallel c$ and $\mathbf{E} \perp c$, respectively. Only one of the possible origins of the observed E₂-type transitions is indicated.

Tables

TABLE I: Values of refractive indices n and extinction coefficients k of CuInSe₂ at intervals of 0.1 eV.

E(eV)	n_{\perp}	k_{\perp}	n_{\parallel}	k_{\parallel}
0.9	2.937		2.950	
1.0	3.048	0.165	3.036	0.179
1.1	3.033	0.314	3.022	0.320
1.2	3.012	0.359	2.990	0.358
1.3	3.003	0.414	2.982	0.406
1.4	2.969	0.460	2.957	0.426
1.5	2.949	0.479	2.938	0.452
1.6	2.935	0.501	2.925	0.479
1.7	2.931	0.519	2.920	0.504
1.8	2.931	0.543	2.916	0.527
1.9	2.933	0.571	2.914	0.550
2.0	2.937	0.604	2.922	0.573
2.1	2.941	0.637	2.936	0.593
2.2	2.949	0.671	2.953	0.625
2.3	2.960	0.712	2.971	0.665
2.4	2.974	0.763	2.998	0.714
2.5	2.983	0.828	3.027	0.773
2.6	2.993	0.908	3.072	0.853
2.7	2.988	1.003	3.125	0.983
2.8	2.951	1.119	3.095	1.223
2.9	2.848	1.225	2.867	1.390
3.0	2.709	1.264	2.635	1.378
3.1	2.620	1.251	2.500	1.271
3.2	2.541	1.236	2.464	1.169
3.3	2.488	1.185	2.475	1.108
3.4	2.479	1.158	2.505	1.092
3.5	2.479	1.164	2.531	1.111
3.6	2.457	1.200	2.531	1.161
3.7	2.390	1.199	2.482	1.181
3.8	2.355	1.159	2.471	1.154
3.9	2.346	1.120	2.495	1.164

4.0	2.366	1.081	2.516	1.207
4.1	2.411	1.061	2.517	1.269
4.2	2.473	1.069	2.482	1.321
4.3	2.536	1.119	2.450	1.352
4.4	2.586	1.194	2.433	1.380
4.5	2.617	1.296	2.410	1.423
4.6	2.613	1.427	2.391	1.468
4.7	2.545	1.562	2.349	1.526
4.8	2.429	1.649	2.299	1.583
4.9	2.319	1.674	2.224	1.628
5.0	2.251	1.672	2.145	1.646
5.1	2.213	1.699	2.092	1.656
5.2	2.154	1.750	2.042	1.688

TABLE II: Values of n and k of CuGaSe₂ at intervals of 0.1 eV.

E(eV)	n_{\perp}	k_{\perp}	n_{\parallel}	k_{\parallel}
1.4	2.904		2.920	
1.5	2.942		2.968	
1.6	3.000		3.054	
1.7	3.082		3.067	0.200
1.8	3.080	0.184	3.048	0.245
1.9	3.102	0.228	3.065	0.276
2.0	3.102	0.294	3.068	0.311
2.1	3.104	0.331	3.076	0.338
2.2	3.116	0.365	3.093	0.364
2.3	3.137	0.392	3.114	0.393
2.4	3.160	0.432	3.139	0.430
2.5	3.188	0.476	3.163	0.472
2.6	3.230	0.522	3.204	0.515
2.7	3.267	0.589	3.251	0.564
2.8	3.306	0.673	3.300	0.640
2.9	3.335	0.784	3.342	0.749
3.0	3.343	0.929	3.387	0.908
3.1	3.318	1.092	3.363	1.162
3.2	3.202	1.246	3.116	1.336
3.3	3.024	1.327	2.876	1.308
3.4	2.879	1.319	2.757	1.193
3.5	2.778	1.297	2.748	1.094
3.6	2.701	1.231	2.784	1.043
3.7	2.700	1.176	2.844	1.036
3.8	2.716	1.161	2.903	1.074
3.9	2.734	1.177	2.945	1.156
4.0	2.733	1.223	2.941	1.277
4.1	2.687	1.253	2.850	1.364
4.2	2.660	1.250	2.796	1.378
4.3	2.650	1.246	2.765	1.412
4.4	2.659	1.242	2.731	1.453
4.5	2.687	1.255	2.689	1.497
4.6	2.725	1.294	2.634	1.529
4.7	2.764	1.372	2.585	1.542
4.8	2.760	1.487	2.546	1.558

4.9	2.705	1.608	2.512	1.582
5.0	2.601	1.706	2.481	1.612
5.1	2.476	1.748	2.443	1.653
5.2	2.343	1.731	2.368	1.698

TABLE III: Values of n and k of CuInS₂ at intervals of 0.1 eV.

E(eV)	n_{\perp}	k_{\perp}	n_{\parallel}	k_{\parallel}
1.4	2.874	0.219	2.866	0.199
1.5	2.945	0.352	2.927	0.341
1.6	2.796	0.422	2.784	0.405
1.7	2.761	0.415	2.748	0.400
1.8	2.742	0.419	2.727	0.408
1.9	2.725	0.437	2.711	0.418
2.0	2.717	0.449	2.705	0.426
2.1	2.708	0.455	2.702	0.431
2.2	2.708	0.469	2.708	0.441
2.3	2.714	0.480	2.715	0.454
2.4	2.721	0.499	2.726	0.471
2.5	2.734	0.523	2.743	0.493
2.6	2.747	0.557	2.767	0.522
2.7	2.764	0.587	2.789	0.555
2.8	2.779	0.635	2.809	0.602
2.9	2.782	0.686	2.821	0.662
3.0	2.783	0.744	2.828	0.733
3.1	2.774	0.807	2.816	0.818
3.2	2.738	0.870	2.767	0.902
3.3	2.686	0.914	2.682	0.955
3.4	2.633	0.940	2.596	0.963
3.5	2.589	0.953	2.545	0.941
3.6	2.556	0.959	2.525	0.920
3.7	2.526	0.959	2.522	0.908
3.8	2.505	0.954	2.524	0.907
3.9	2.493	0.949	2.534	0.919
4.0	2.486	0.951	2.540	0.944
4.1	2.485	0.949	2.535	0.972
4.2	2.502	0.950	2.533	0.997
4.3	2.521	0.961	2.529	1.024
4.4	2.548	0.992	2.525	1.059
4.5	2.567	1.037	2.516	1.095
4.6	2.580	1.094	2.507	1.130
4.7	2.581	1.160	2.499	1.170
4.8	2.557	1.230	2.480	1.216
4.9	2.527	1.303	2.460	1.268
5.0	2.477	1.366	2.424	1.318
5.1	2.410	1.410	2.381	1.364

5.2	2.343	1.440	2.314	1.387
-----	-------	-------	-------	-------

TABLE IV: Values of n and k of CuGaS₂ at intervals of 0.1 eV.

E(eV)	n_{\perp}	k_{\perp}	n_{\parallel}	k_{\parallel}
1.4	2.579		2.574	
1.5	2.590		2.588	
1.6	2.604		2.604	
1.7	2.623		2.624	
1.8	2.646		2.647	
1.9	2.675		2.677	
2.0	2.706		2.711	
2.1	2.742		2.753	
2.2	2.779		2.800	
2.3	2.822		2.858	0.108
2.4	2.874	0.101	2.891	0.222
2.5	2.918	0.207	2.846	0.262
2.6	2.888	0.270	2.842	0.279
2.7	2.884	0.301	2.847	0.297
2.8	2.890	0.325	2.859	0.316
2.9	2.901	0.348	2.876	0.334
3.0	2.929	0.374	2.898	0.361
3.1	2.955	0.411	2.926	0.391
3.2	2.977	0.453	2.954	0.427
3.3	3.003	0.505	2.985	0.474
3.4	3.028	0.567	3.016	0.534
3.5	3.048	0.646	3.045	0.611
3.6	3.053	0.733	3.054	0.709
3.7	3.036	0.823	3.026	0.813
3.8	2.996	0.912	2.962	0.885
3.9	2.935	0.975	2.900	0.913
4.0	2.871	1.014	2.869	0.922
4.1	2.823	1.033	2.860	0.938
4.2	2.787	1.043	2.862	0.974
4.3	2.769	1.058	2.855	1.029
4.4	2.756	1.084	2.836	1.083
4.5	2.738	1.120	2.804	1.140
4.6	2.715	1.161	2.769	1.193
4.7	2.682	1.191	2.714	1.238
4.8	2.662	1.219	2.668	1.268
4.9	2.632	1.264	2.618	1.295
5.0	2.591	1.293	2.584	1.317
5.1	2.550	1.305	2.541	1.343
5.2	2.538	1.329	2.507	1.380

TABLE V: Characteristic parameters of the fundamental gap of studied Cu-III-VI₂ compounds. All energies are given in eV and the numbers in parentheses indicate the error margin of the last given decimal. Unless otherwise indicated data are results at room temperature.

	CuInSe ₂		CuGaSe ₂			CuInS ₂		CuGaS ₂		
	This work	Ref. 35 (77 K)	This work	Ref. 36	Ref. 37	This work	Ref. 36 (2 K)	This work	Ref. 38	Ref. 38 (20 K)
$E_0(A)$	1.04(1)	1.038	1.648(2)	1.68	1.686	1.530(5)	1.55	2.411(2)	2.469	2.497

$E_0(B)$	1.039(3)	1.042	1.717(4)	1.76	1.760	1.530(5)	2.530(4)	2.597	2.625
$E_0(C)$	1.274(6)	1.273	1.920(6)	1.96	1.972				2.635
$-\Delta_{cf}$		-0.006	0.093	0.094	0.099		0.119	0.128	0.132
Δ_{so}	0.235	0.233	0.227	0.234	0.237		-0.02		-0.016

TABLE VI: Selection rules of the dipolar interband transitions at the main points of the Brillouin zone of the chalcopyrite structure.

BZ point	$\mathbf{E} \parallel c$ (Γ_4)	$\mathbf{E} \perp c$ (Γ_5)
Γ	$\Gamma_1 \otimes \Gamma_4$	$\Gamma_1 \otimes \Gamma_5$
	$\Gamma_2 \otimes \Gamma_3$	$\Gamma_2 \otimes \Gamma_5$
	$\Gamma_5 \otimes \Gamma_5$	$\Gamma_3 \otimes \Gamma_5$
T	$(T_1 + T_2) \otimes (T_3 + T_4)$	$(T_1 + T_2) \otimes T_5$
	$T_5 \otimes T_5$	$(T_3 + T_4) \otimes T_5$
N	$N_1 \otimes N_1$	$N_1 \otimes N_1$

TABLE VII: Fitted upper transition energies (in eV) and their polarization for the two studied selenides. The numbers in parentheses indicate the error margin of the last given decimal.

Label	CuInSe ₂		CuGaSe ₂	
	$\mathbf{E} \parallel c$	$\mathbf{E} \perp c$	$\mathbf{E} \parallel c$	$\mathbf{E} \perp c$
$E(\Gamma X)$		2.4(1)		2.8(1)
		2.5 ^a		
$E_1(A)$	2.821(4)	2.901(5)	3.127(2)	3.247(5)
	2.92 ^a	2.92 ^a	3.28 ^b	3.28 ^b
	2.92 ^c	2.92 ^c	3.08 ^c	3.08 ^c
$E(X\Gamma)$		3.174(5)		3.501(4)
		3.24 ^a		3.35 ^b
$E_1(B)$	3.635(5)	3.626(5)	4.049(5)	4.03(1)
	3.72 ^a	3.72 ^a	4.20 ^b	4.16 ^b
	3.65 ^c	3.65 ^c		
$E(\Delta X)$	4.07(5)		4.49(5)	
	4.2 ^a			
	4.15 ^c			
$E'(\Gamma X)$		4.2(1)		
		4.4 ^a		

$E_2(A)$	4.71(2)	4.89(5)
	4.85 ^a	
	4.70 ^c	
$E_2(B)$	4.84(4)	5.1(1)
	4.85 ^a	5.0 ^c
	4.90 ^c	

^aRef. 21 (80 K)

^bRef. 22 (80 K)

^cRef. 12

TABLE VIII: Main optical transition energies (in eV) and their polarization measured above the fundamental edge in Cu-III-S₂. The numbers in parentheses indicate error margins.

Label	CuInS ₂		CuGaS ₂	
	$\mathbf{E} \parallel c$	$\mathbf{E} \perp c$	$\mathbf{E} \parallel c$	$\mathbf{E} \perp c$
$E(\Gamma X)$		2.75(8)		3.5(1)
	3.099 ^a	3.087 ^a		
$E_1(A)$	3.27(1)	3.27(5)	3.720(5)	3.85(1)
	3.247 ^a	3.246 ^a	3.84 ^b	3.28 ^b
$E(X\Gamma)$	3.6(1)	3.5(1)		
	3.655 ^a	3.669 ^a		4.20 ^b
$E(\Delta X)$			4.15(5)	
			4.40 ^b	
$E_1(B)$	3.94(5)	3.9(1)	4.63(1)	4.53(1)
	4.053 ^a	4.091 ^a	4.70 ^b	4.68 ^b
$E'(\Gamma X)$	4.4(1)	4.4(2)		
$E_2(A)$	4.8(1)	4.7(1)		4.91(1)
	5.038 ^a			5.12 ^b
$E_2(B)$	5.09(3)	5.05(3)		
		5.033 ^a	5.14 ^b	

^aRef. 24 (77 K)

^bRef. 19 (80 K)

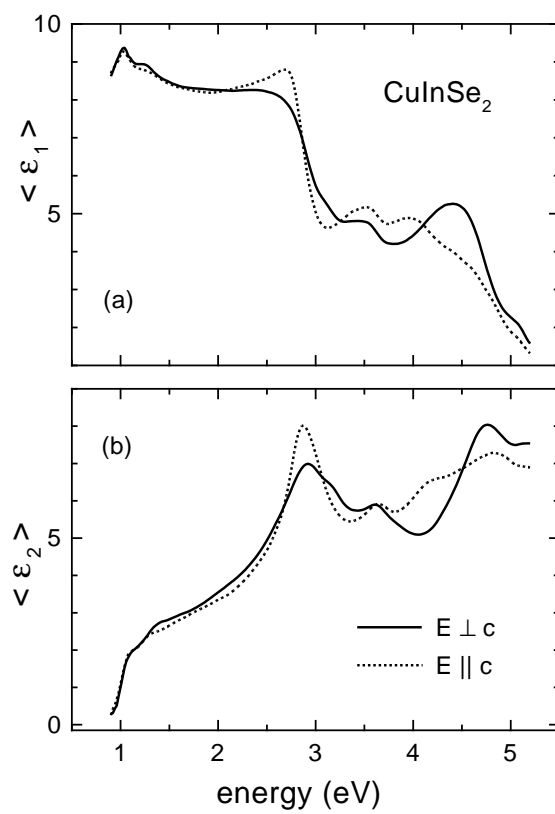


FIGURE 1 (Alonso et al.)

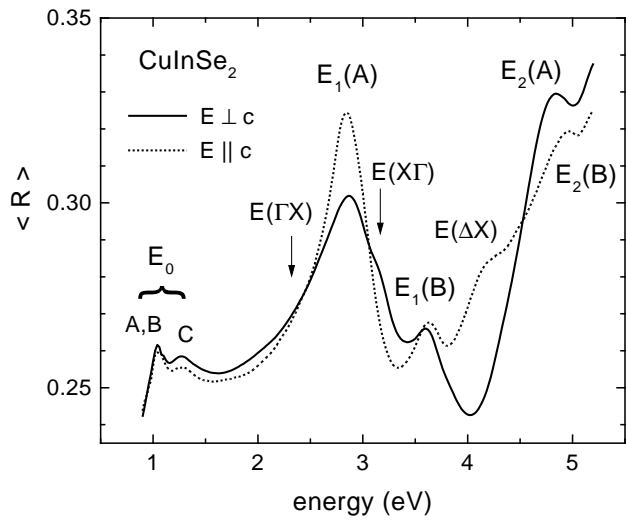


FIGURE 2 (Alonso et al.)

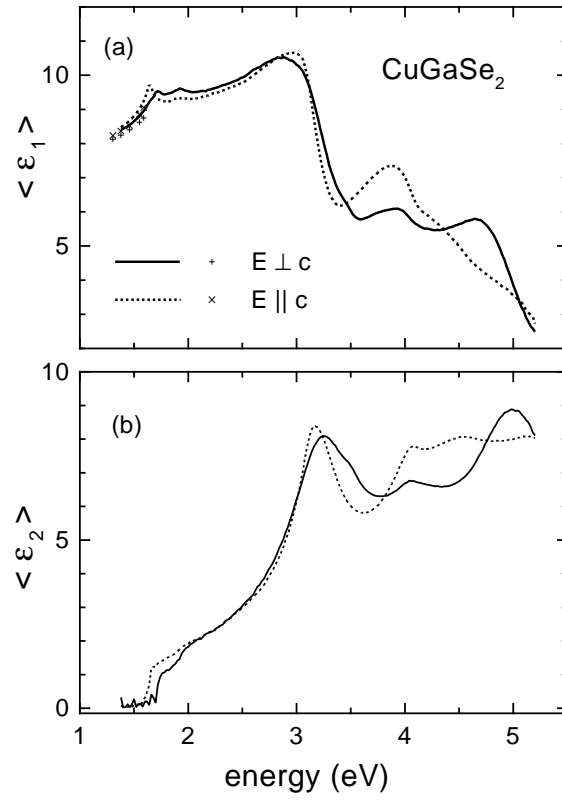


FIGURE 3 (Alonso et al.)

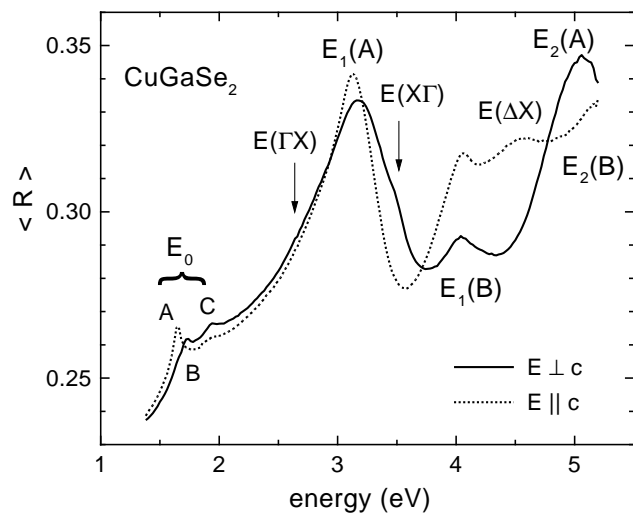


FIGURE 4 (Alonso et al.)

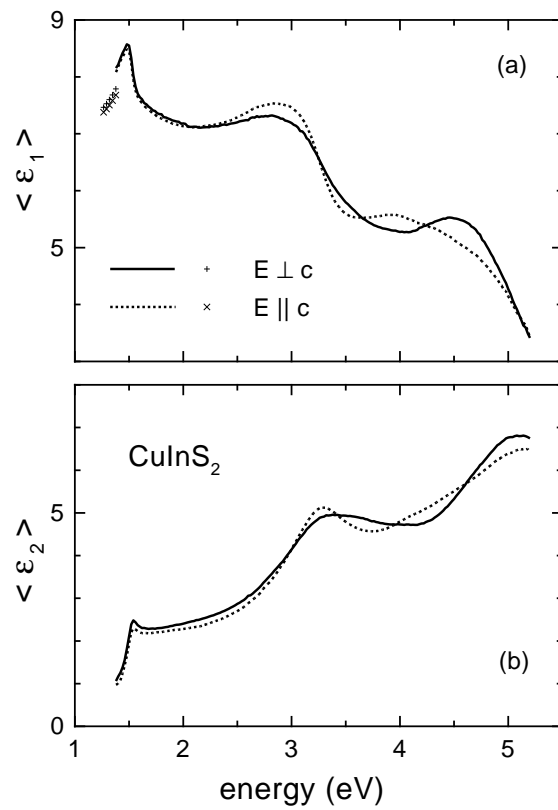


FIGURE 5 (Alonso et al.)

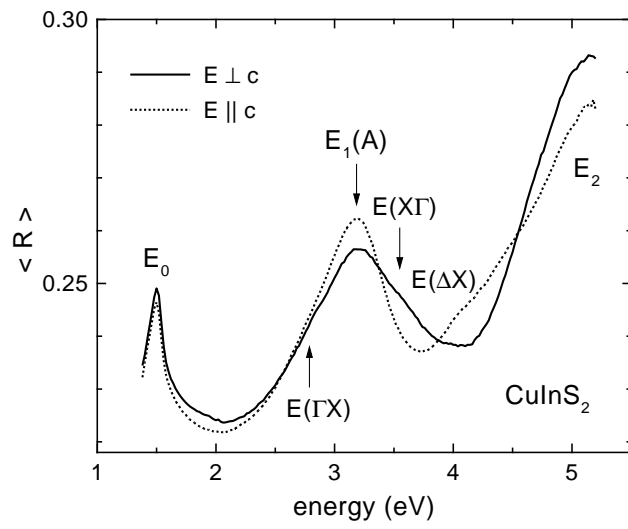


FIGURE 6 (Alonso et al.)

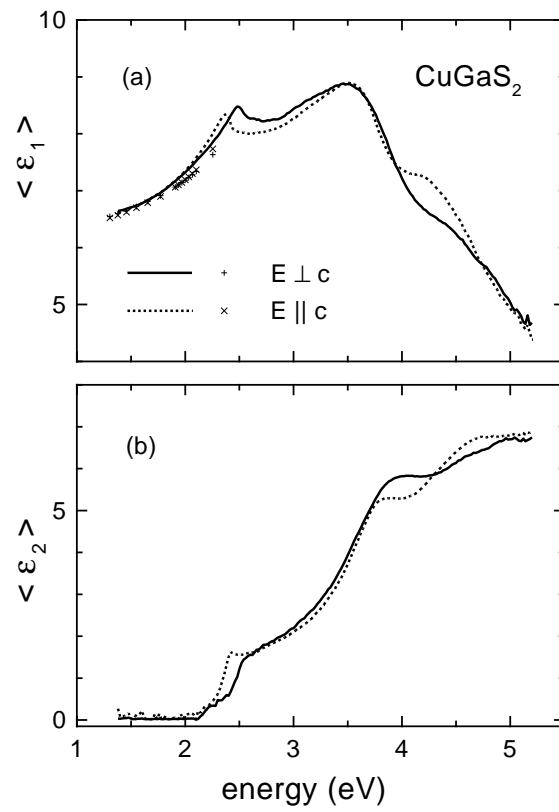


FIGURE 7 (Alonso et al.)

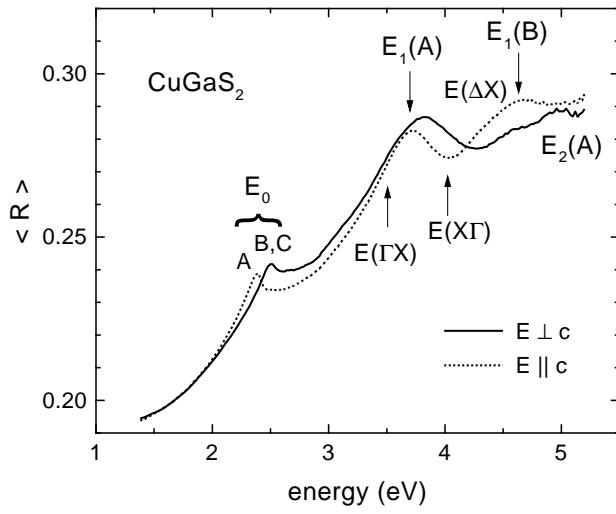


FIGURE 8 (Alonso et al.)

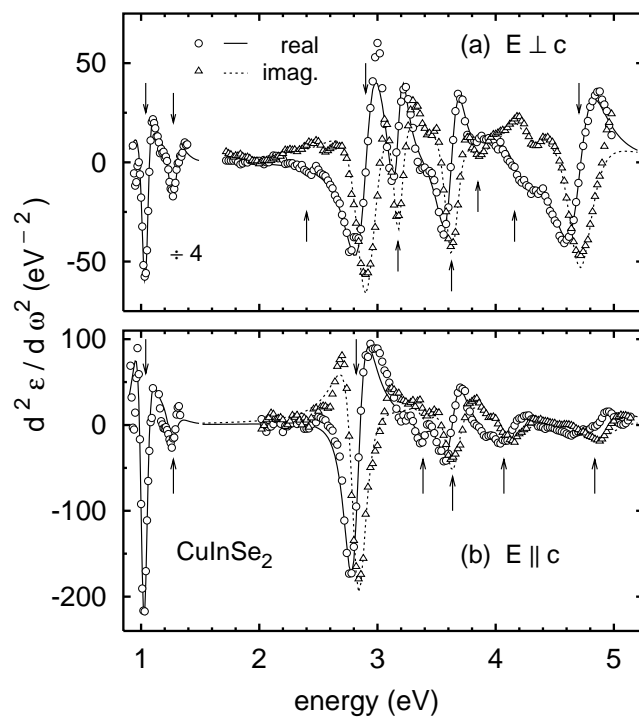


FIGURE 9 (Alonso et al.)

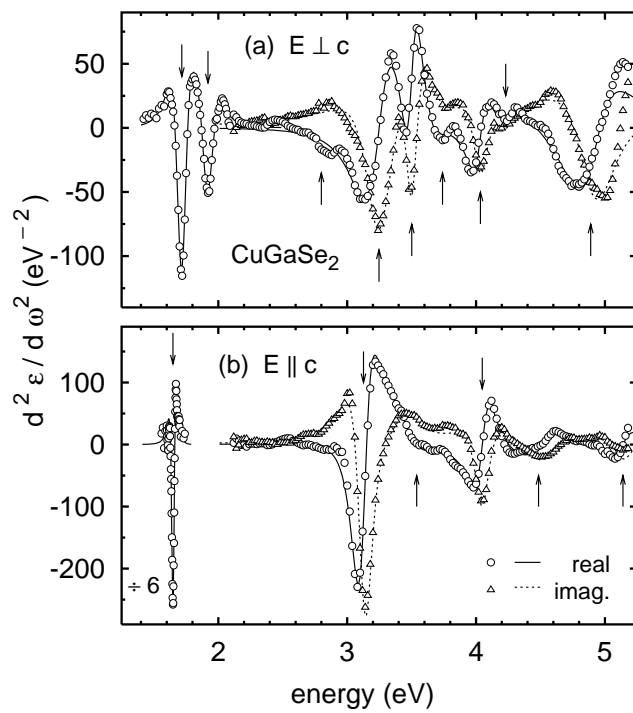


FIGURE 10 (Alonso et al.)

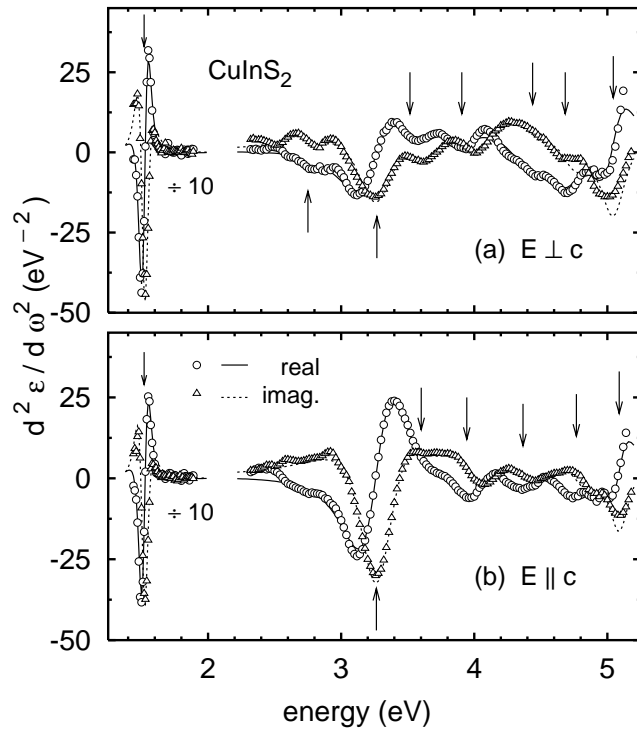


FIGURE 11 (Alonso et al.)

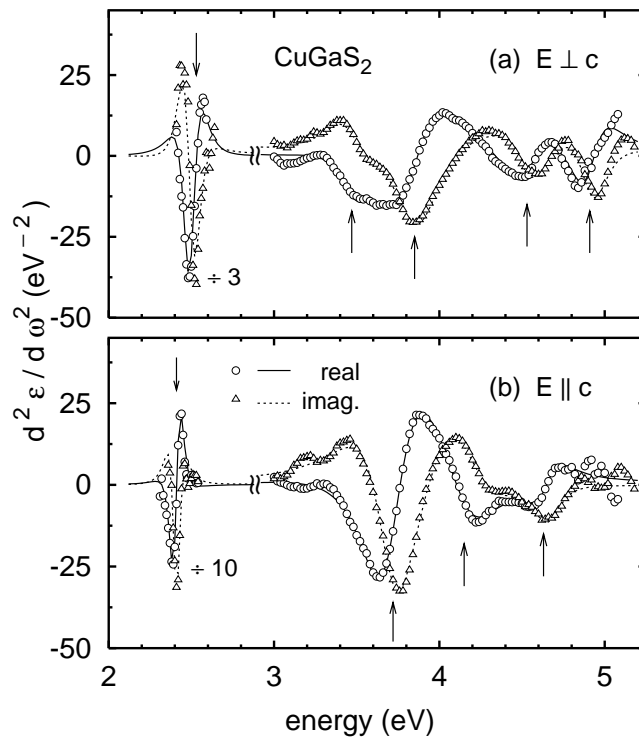


FIGURE 12 (Alonso et al.)

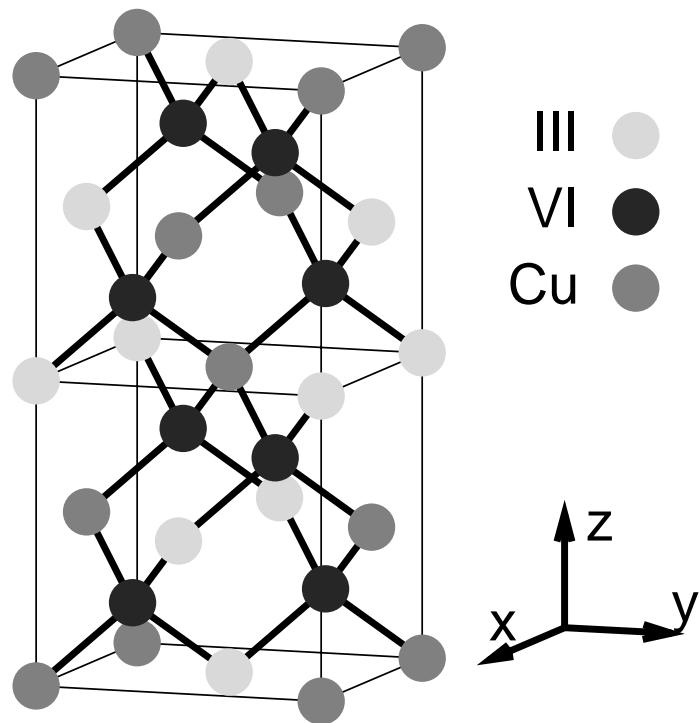


FIGURE 13 (Alonso et al.)

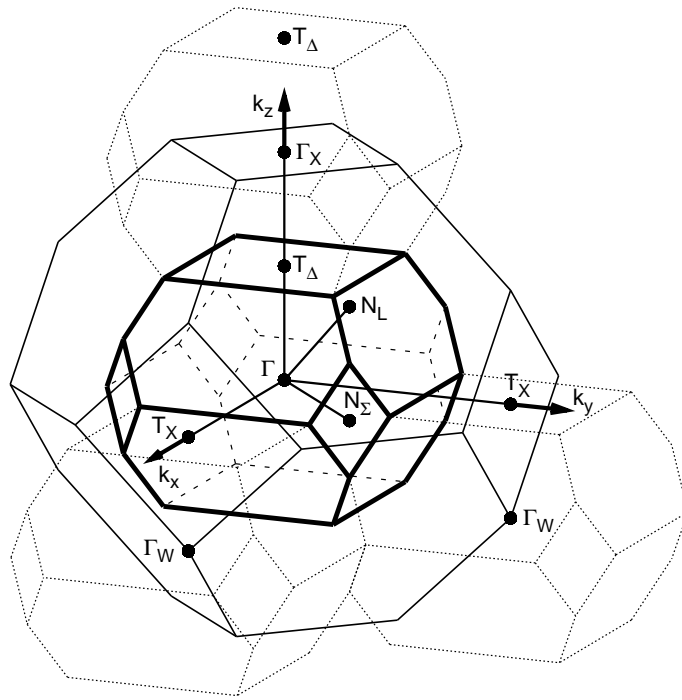


FIGURE 14 (Alonso et al.)

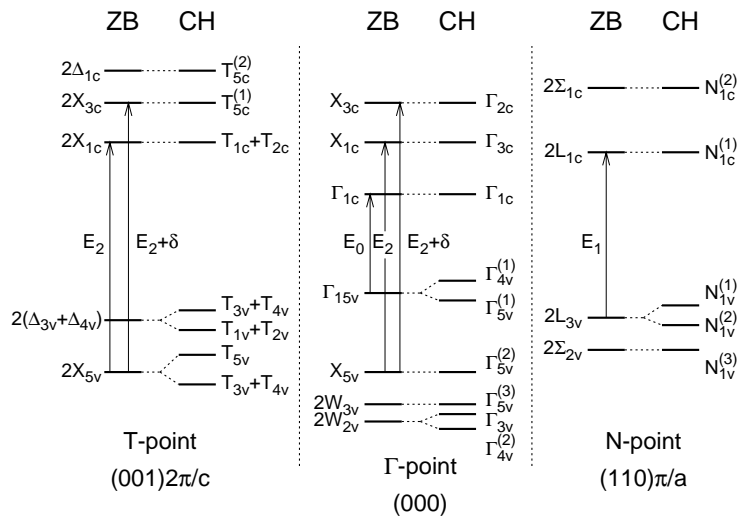


FIGURE 15 (Alonso et al.)

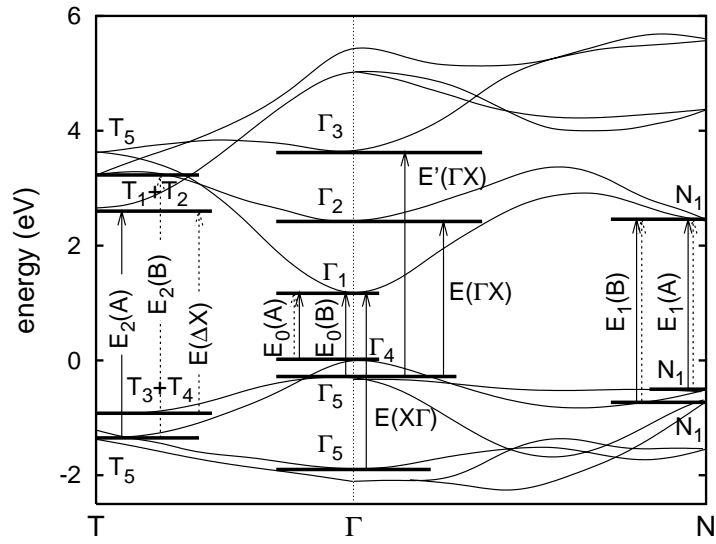


FIGURE 16 (Alonso et al.)